

Fluid flow in thin fractured porous media using a TPM-phase-field model and microfluidic experiments

Yann Rivas

University of Stuttgart

Nikolaos Karadimitriou

University of Stuttgart

Holger Steeb

University of Stuttgart

Wolfgang Ehlers

University of Stuttgart

Arndt Wagner

arndt.wagner@mechbau.uni-stuttgart.de

University of Stuttgart

Research Article

Keywords:

Posted Date: March 20th, 2025

DOI: <https://doi.org/10.21203/rs.3.rs-6077893/v1>

License:  This work is licensed under a Creative Commons Attribution 4.0 International License.

[Read Full License](#)

Additional Declarations: No competing interests reported.

Fluid flow in thin fractured porous media using a TPM-phase-field model and microfluidic experiments

Yann Rivas¹ · Nikolaos Karadimitriou¹ ·
Holger Steeb^{1,2} · Wolfgang Ehlers¹ ·
Arndt Wagner^{1,*}

Received: date / Accepted: date

Abstract The Theory of Porous Media (TPM) with an embedded phase-field approach to fracture provides an elegant opportunity to study complex flow phenomena in fractured porous materials in a unified single-domain approach. On this basis, the interactive flow behaviour between free flow and porous-media flow is studied using the example of flow through a thin porous plate containing a rectangular channel. By considering different boundary conditions and investigating the flow behaviour for a range of hydraulic conductivities, our study is designed to reveal insights into phenomena which are relevant for various sub-surface geo-engineered applications. Furthermore, we show that the applied macroscopic single-domain approach is able to reveal local flow effects near the porous interface (channel walls), namely the so-called velocity profile inversion phenomenon. Moreover, we introduce a geometrically motivated estimation of the length-scale parameter ϵ used in phase-field approaches, which is directly related to the roughness of the fracture surface. Thus, values for ϵ are proposed for microfluidic devices and different rock types. Furthermore, we apply full three-dimensional simulations to evaluate the influence of the thickness of thin porous plates on the overall flow resistance, which is typically relevant in microfluidic devices. In a combined numerical-experimental study, we compare results from representative microfluidic experiments and simulations and confirmed the choice of ϵ to correctly predict the flow transition across the porous interface.

¹ Yann Rivas, Nikolaos Karadimitriou, Holger Steeb, Wolfgang Ehlers, Arndt Wagner
University of Stuttgart, Institute of Applied Mechanics, Pfaffenwaldring 7, 70569 Stuttgart,
Germany

² Holger Steeb
University of Stuttgart, Stuttgart Center for Simulation Science (SC SimTech), Pfaffen-
waldring 5a, 70569 Germany

*Corresponding author: Arndt Wagner
University of Stuttgart, Institute of Applied Mechanics, Pfaffenwaldring 7, 70569 Stuttgart,
Germany. E-mail: arndt.wagner@mechbau.uni-stuttgart.de

Keywords Porous media · Fractures · TPM · Phase-field method · Diffuse interface · Microfluidics · Coupled flow

1 Introduction

The understanding of coupled flow processes occurring in the transition zone between free flow and porous-media flow is of crucial importance in many engineering fields, ranging from geo- and bio-mechanical applications to engineered technical systems, such as geothermal energy plants, vascular tissues or fuel cells.

In general, a fractured porous material can be divided into an intact and a naturally or artificially fractured region, cf. Figure 1 (left). In these two domains, typical characteristic flow phenomena occur. To describe these flow phenomena, various modelling approaches in different length scales exist. For example, the flow behaviour in an intact porous material can be described macroscopically using the famous Darcy's law [9], which assumes, among others, creeping flow conditions with negligible accelerations. For higher fluid velocities, the Forchheimer equation [18] provides an extension of Darcy's law including a quadratic velocity term which considers a pressure loss due to high velocities and, furthermore, an additional parameter accounting for the tortuosity of the microscopic pore-network architecture, cf. Bear [2]. For a detailed overview on the macroscopic, continuum-mechanical description of flow in intact porous media, the interested reader is further referred to the works of Coussy [8], Helmig [24] and Ehlers [12].

In a fractured porous material, one can further distinguish between an open and a closed fracture, cf. Ehlers & Luo [14]. In this regard, flow in a closed fracture can still be described by means of a porous-media flow, whereas in an open fracture, free fluid-flow conditions are given. In classical fluid mechan-

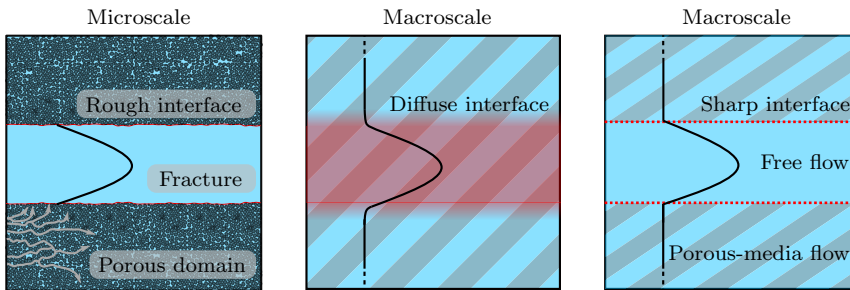


Fig. 1: Modelling approaches for coupled flow phenomena. From left to right: Fully resolved porous domain with fracture, single-domain approach on the macroscale including a phase-field for the diffuse fracture description, and a classic two-domain approach with a sharp interface coupling between free flow and porous-media flow.

ics, the free flow of a fluid through a channel or a pipe is described by the continuum-mechanical Navier-Stokes equation, comprehensively discussed in textbooks such as the ones of von Böckh & Saumweber [5] or Sigloch [38]. In the case of creeping flow (Reynolds number $Re < 1$), the inertial forces are small compared to the viscous forces and can therefore be neglected. The resulting Stokes equation is one example of possible simplifications which are often used for simulations of connected pore networks, cf. Krach et al. [28]. Therein, the geometrically resolved porous domain (macroscale) depends on the underlying physical behaviour of the fluid on the pore scale (microscale) and includes a scale linking. As an overview, a comprehensive summary of methods for describing flow in fractured porous media is provided by Berre et al. [4].

To study flow phenomena on the pore scale, one can either use experiments, e.g. microfluidic experiments as described in Karadimitriou et al. [27] in combination with Particle Image Velocimetry (PIV) measurements, cf. Terzis et al. [43], or pore-scale models which describe the pore-resolved flow processes. The gained information can then be taken to verify assumptions or estimate material parameters for the macroscopic approaches, cf. Wagner et al. [45].

Proceeding to the modelling of the transition between two flow regimes, specific model-dependent challenges regarding their meaningful coupling arise. In this regard, there exist so-called single-domain or two-domain approaches, cf. Figure 1. A single-domain approach solves a single set of coupled equations for the complete domain with either continuous, cf. Goyeau et al. [20] and Valdés-Parada et al. [44], or discontinuous variation of physical properties, cf. Silva et al. [39, 40], such as the hydraulic conductivity or porosity. To name an example, the standard Darcy-Brinkman equation, cf. Brinkman [6], results in either a Stokes-type flow for high hydraulic conductivities or a Darcy-type flow for low hydraulic conductivities. In contrast, a two-domain approach couples two different flow types such as Stokes flow and Darcy flow at a sharp interface via suitable coupling conditions. Typically, these are based on the conservation of mass and momentum, as proposed in the fundamental works of Beaver & Joseph [3] and Saffman [37] and more recent contributions, e.g., Rybak et al. [36] or Strohbeck et al. [42]. However, the above mentioned two-domain approaches encounter difficulties in modelling the transition zone between the two flow regimes since a physically feasible choice for the individual model parameters, the location of the interface and fitting coupling conditions need to be considered.

To avoid these difficulties, the Theory of Porous Media (TPM) with an embedded phase-field approach to fracture has been proven useful in describing coupled fluid-flow phenomena over diffuse interfaces and therefore provides an elegant single-domain approach. In this contribution, we mainly refer to the works of Ehlers & Luo [13, 14] and related works of Kuhn et al. [30], Miehe et al. [32] and Heider et al. [23]. Apart from the convenient properties of the model, this choice is also based on the fact that the group around Wolfgang Ehlers has a long history and experience in this area and made a number of significant contributions in recent years, cf. Ehlers et al. [15], Wagner et

al. [46], Sonntag et al. [41] or Wang et al. [47]. A key feature of the TPM phase-field approach is that the momentum equation of the liquid is able to switch between a Darcy-type or a Navier-Stokes-type equation depending on the local fracturing state of the solid that is governed by the single scalar phase-field variable ϕ^S . Moreover, the transition length from fractured to unfractured material is governed by the length-scale parameter ϵ . In this diffuse interface approach, one heads towards the rather theoretical (mathematical) sharp-interface approach for ϵ towards zero. However, it is physically reasonable to use a certain diffuseness of the interface, in particular for applications. Since no specific attention has yet been paid to study ϵ with regard to coupled flow regimes, this is one main focus in this contribution. Using a combined numerical and experimental investigation, we will present reliable theoretical assumptions and confirm them with tailor-made microfluidic experiments.

In particular, the manuscript is structured as follows. In Section 2, the modelling and simulation approach is presented. For this, the considered TPM-phase-field model of Ehlers & Luo [13] is briefly introduced and theoretically discussed in Section 2.1 with special attention paid to the fluid behaviour relevant for the focused research questions. In this regard, the estimation of the length-scale parameter ϵ for specific fracture surface topologies is discussed in Section 2.2. In Section 3, the setup of a general numerical study of a thin porous plate containing a straight rectangular channel is introduced and the numerical results are discussed. Therein, we study in Section 3.2 the coupled fluid-flow behaviour arising at the porous interface for two different boundary conditions and a wide range of hydraulic conductivities relevant for various sub-surface geo-engineering issues. Furthermore, we show in Section 3.3 that the TPM-phase-field model is even able to capture very detailed effects, such as the widely known “velocity profile inversion”. In contrast to Reci et al. [35] and Haustein & Kashi [21] discussing flow within impermeable boundaries, we were here able, for the first time, to discuss the phenomenon for a free-flow channel with porous boundaries (interfaces). Moreover, in Section 3.4 the influence of the thickness of thin fractured porous media on the flow resistance is evaluated and the importance of fully three-dimensional simulations is revealed. This preparatory numerical study motivated the challenging fabrication of microfluidic samples with a reasonable thickness for tailored microfluidic experiments for validation purposes. In addition, the role of solid deformations is evaluated for the conducted microfluidic experiments. In Section 4, the results of the combined numerical-experimental study is presented. This includes the specific production of appropriate microfluidic chips and the customised experimental setup in Section 4.1 and Section 4.2, respectively. On this basis, the estimation of hydraulic conductivities and local velocity fields using pressure measurements and particle imaging velocimetry (PIV) is described in detail. Subsequently, the experimental data and the determination of material parameters for the related numerical simulation of the microfluidic chips are shown in Section 4.3. Overall, we were able to verify our choice of the length-scale parameter ϵ and at the same time showed the predictive ca-

pabilities of the TPM-phase-field model. Finally, this manuscript concludes in Section 5 with a detailed discussion of the findings.

2 Modelling and simulation approach

2.1 Biphasic TPM model for fractured porous media

In this section, the well established biphasic porous-media model with an embedded phase-field to describe diffuse fractures is briefly summarised with a specific focus on the issues of coupled fluid-flow phenomena. For a more comprehensive insight in the phase-field-based modelling approach, the interested reader is referred to the fundamental works of Ehlers & Luo [13, 14] or Heider & Markert [22].

2.1.1 Basic model setup

The considered biphasic model is based on the works of Ehlers & Luo [13, 14], where a linear-elastic porous solid skeleton φ^S is considered fully saturated with a single incompressible viscous liquid φ^L . The TPM provides a macroscopic description of this biphasic aggregate via

$$\varphi = \bigcup_{\alpha} \varphi^{\alpha} = \varphi^S \cup \varphi^L \quad \text{with} \quad \alpha = \{S, L\} \quad (1)$$

as superimposed and mutually interacting continua with individual motion functions, cf., e.g., Ehlers [11] for a comprehensive overview on the TPM. In terms of the underlying volume averaging, the so-called representative elementary volume (REV) acts as a control volume which captures a large enough space of the porous domain, allowing for a meaningful local averaging process for the constituent's properties. To quantify the amount of each constituent on the local volume element dv , the concept of volume fractions is introduced as

$$n^{\alpha} := \frac{dv^{\alpha}}{dv}, \quad \text{such that} \quad n^S + n^L = 1. \quad (2)$$

Therein, dv^{α} is the local volume element of a constituent φ^{α} , while (2)₂ is known as the saturation condition. Strongly connected, the partial density ρ^{α} and the real density $\rho^{\alpha R}$ of the constituents are found by comparing the local mass element dm^{α} to either the partial volume element dv^{α} or the (total) volume element dv , yielding

$$\rho^{\alpha R} = \frac{dm^{\alpha}}{dv^{\alpha}} \quad \text{and} \quad \rho^{\alpha} = \frac{dm^{\alpha}}{dv} \quad \rightarrow \quad \rho^{\alpha} = n^{\alpha} \rho^{\alpha R}. \quad (3)$$

Within the TPM, the motion of the porous solid skeleton is described in a Langrangean setting via the deformation vector \mathbf{u}_S as the basic variable for the solid velocity \mathbf{v}_S , the solid deformation gradient \mathbf{F}_S and the linearised solid strain tensor $\boldsymbol{\varepsilon}_S$. Describing a biphasic material, the solid skeleton contains the

pore liquid in a hierarchical manner, meaning that the liquid is percolating through a deforming porous solid acting as its reference system. This leads to a modified Eulerian description of the liquid using the seepage velocity \mathbf{w}_L relating the absolute liquid velocity \mathbf{v}_L to the velocity \mathbf{v}_S of the deforming solid skeleton. The underlying individual motion or placement function χ_α of a material point of the studied biphasic aggregate describes the current position \mathbf{x} at time t with respect to the individual reference position \mathbf{X}_α at the initial time t_0 . This leads to the following basic kinematical description of the constituents, viz.:

$$\mathbf{x} = \chi_\alpha(\mathbf{X}_\alpha, t) \rightarrow \begin{cases} \mathbf{u}_S = \mathbf{x} - \mathbf{X}_\alpha, \quad \mathbf{v}_S = \dot{\mathbf{x}}_S = (\mathbf{u}_S)'_S = (\chi_\alpha)'_S, \\ \mathbf{F}_S = \frac{\partial \mathbf{x}}{\partial \mathbf{X}_\alpha} = \text{Grad}_S \mathbf{x}, \\ \boldsymbol{\epsilon}_S = \frac{1}{2}(\text{Grad}_S \mathbf{u}_S + \text{Grad}_S^T \mathbf{u}_S), \\ \mathbf{v}_L = (\chi_L)'_L, \quad \mathbf{w}_L = \mathbf{v}_L - \mathbf{v}_S, \\ \mathbf{D}_L = \frac{1}{2}(\text{grad} \mathbf{v}_L + \text{grad}^T \mathbf{v}_L). \end{cases} \quad (4)$$

Herein, $(\cdot)'_\alpha$ denotes the material time derivative with respect to the motion of the constituent φ^α , while $\partial(\cdot)/\partial \mathbf{X}_\alpha = \text{Grad}_\alpha(\cdot)$ and $\partial(\cdot)/\partial \mathbf{x} = \text{grad}(\cdot)$ are the gradient operators related to the referential and the current configuration. \mathbf{D}_L is the deformation velocity of the liquid.

2.1.2 Phase-field description of diffuse fractures

The phase-field approach applied to fracturing porous materials originates from an energetic formulation depending on the so-called phase-field variable ϕ^S that describes the state of the solid, cf., e.g., the articles of Miehe et al. [32], Kuhn & Müller [30] or Ehlert & Luo [13, 14] and citations therein. In particular, the state of the solid is between intact ($\phi^S = 0$) and fully fractured ($\phi^S = 1$), which leads to a binary limitation of the phase-field variable, viz.:

$$0 \leq \phi^S \leq 1. \quad (5)$$

In order to accurately describe propagating fractures, an evolution equation of the phase-field variable ϕ^S was proposed by Miehe et al. [33] that contains the history $\mathcal{H} = \max\{W^{S+}\}$ of the positive part W^{S+} (tensile energy) of the solid strain energy W^S . This evolution is of Ginzburg-Landau type reading

$$(\phi^S)'_S = \frac{1}{M} [2(1 - \phi^S)\mathcal{H} - \frac{G_c}{\epsilon}(\phi^S - \epsilon^2 \text{div grad} \phi^S)]. \quad (6)$$

Therein, $\text{div}(\cdot)$ is the divergence operator corresponding to $\text{grad}(\cdot)$, while G_c describes the fracture toughness of the porous solid per unit fractured area, $M > 0$ is the mobility parameter, and ϵ a length-scale parameter governing the fracture diffusity. The transition from a fully fractured to an intact state can be displayed via,

$$\phi_{[0,1]}^S = \exp(-|x|/\epsilon). \quad (7)$$

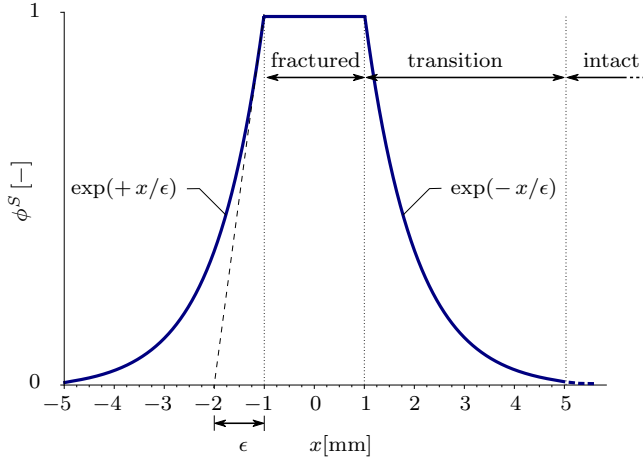


Fig. 2: Schematic one-dimensional sketch of the phase field in the context of a diffuse fracture approach for an exemplary length-scale parameter of $\epsilon = 1$ mm.

The above equation describes the diffuse fracture topology resulting from the phase-field approach to fracture. Therein, the width x characterises the transition between $\phi^S = 1$ and $\phi^S = 0$ towards the asymptotic limit. This transition width is regulated by the length-scale parameter ϵ , cf. Figure 2. Following the idea of a fully open static fracture existing throughout the whole investigated process, the phase-field variable has to be constant in space and time in the fractured domain. As a result, $(\phi^S)'_S$ and $\operatorname{div} \operatorname{grad} \phi^S$ vanish, and the evolution equation can be solved for $\mathcal{H} = \mathcal{H}_0$ yielding

$$\mathcal{H}_0 = \frac{G_c \phi^S}{2 \epsilon (1 - \phi^S)}, \quad (8)$$

cf. Sonntag et al. [41]. Since \mathcal{H}_0 would aim for an infinite value in the limiting case $\phi^S \rightarrow 1$, a value very close to one is typically chosen. Additionally, it is important to note that for a static, non-evolving fracture the mobility parameter M has no contribution to the physical behaviour. At the same time, this also applies to the fracture toughness G_c which, apart from setting an appropriate \mathcal{H}_0 , does not further contribute to the problem.

2.1.3 Balance equations

For standard Cauchy continua in an isothermal setting, we consider material incompressibility through $\rho^{\alpha R} = \text{const.}$ and exclude mass-exchange processes between both constituents, solid and pore liquid, such that the following volume and momentum balance equations are obtained (Ehlers [11]):

$$\begin{aligned} (\rho^\alpha)'_\alpha + \rho^\alpha \operatorname{div}' \dot{\mathbf{x}}_\alpha &= 0 \quad \longrightarrow \quad (n^\alpha)'_\alpha + n^\alpha \operatorname{div}' \dot{\mathbf{x}}_\alpha = 0, \\ \rho^\alpha \ddot{\mathbf{x}}_\alpha &= \operatorname{div} \mathbf{T}^\alpha + \rho^\alpha \mathbf{g} + \hat{\mathbf{p}}^\alpha \quad \text{with} \quad \sum_\alpha \hat{\mathbf{p}}^\alpha = \mathbf{0}. \end{aligned} \quad (9)$$

In (9)₂, \mathbf{T}^α is the symmetric partial Cauchy stress, $\hat{\mathbf{p}}^\alpha$ defines the direct momentum production or the local interaction force, respectively, while \mathbf{g} is the gravitation vector.

2.1.4 Constitutive setting

Basic considerations: By use of thermodynamic restrictions and a rigorous modelling approach for TPM formulations as was shown in Ehlers & Luo [13, 14], the entropy inequality, or more precisely, the Clausius-Planck inequality for isothermal processes yields

$$\sum_{\alpha} [\mathbf{T}^\alpha \cdot \mathbf{D}_\alpha - \rho^\alpha (\psi^\alpha)'_\alpha - \hat{\mathbf{p}}^\alpha \cdot \dot{\mathbf{x}}_\alpha] \geq 0. \quad (10)$$

This inequality, where ψ^α defines the mass-specific Helmholtz energy, acts as the basis for the exploitation of thermodynamic restrictions for all necessary constitutive equations. In the framework of fully or partially saturated fracturing porous media, compare Ehlers & Luo [13, 14] and Sonntag et al. [41], the following results are valid for the problem under study:

$$\mathbf{T}^\alpha = -n^\alpha p \mathbf{I} + \mathbf{T}_E^\alpha, \quad \hat{\mathbf{p}}^\alpha = p \operatorname{grad} n^\alpha + \hat{\mathbf{p}}_E^\alpha. \quad (11)$$

Therein, p is the pore pressure acting everywhere in the porous medium, while \mathbf{T}_E^α and $\hat{\mathbf{p}}_E^\alpha$ are the extra terms of stresses and momentum productions acting in the particular partial bodies, solid and pore liquid. Thereby, \mathbf{T}_E^S defines the solid extra or effective stress governed by the solid deformation through $\boldsymbol{\varepsilon}_S$, while \mathbf{T}_E^L characterises the liquid extra or frictional stress depending on the liquid deformation velocity \mathbf{D}_L . Furthermore, $\hat{\mathbf{p}}_E^L = -\hat{\mathbf{p}}_E^S$ is the extra term of the direct momentum production governed by the seepage velocity $\mathbf{w}_L = \mathbf{v}_L - \mathbf{v}_S$.

Elastic solid with fracture: For fractured porous media with small deformations, the effective solid stress reads

$$\begin{aligned} \mathbf{T}_E^S = & [(1 - \phi^S)^2 + \eta_r^S] \left[2\mu^S \boldsymbol{\varepsilon}_S^+ + \lambda^S \left(\frac{\operatorname{tr} \boldsymbol{\varepsilon}_S + |\operatorname{tr} \boldsymbol{\varepsilon}_S|}{2} \right) \mathbf{I} \right] \\ & + 2\mu^S \boldsymbol{\varepsilon}_S^- + \lambda^S \left(\frac{\operatorname{tr} \boldsymbol{\varepsilon}_S - |\operatorname{tr} \boldsymbol{\varepsilon}_S|}{2} \right) \mathbf{I}. \end{aligned} \quad (12)$$

Therein, $\boldsymbol{\varepsilon}_S^+$ and $\boldsymbol{\varepsilon}_S^-$ are the tensile and compressive eigentensors of $\boldsymbol{\varepsilon}_S$ yielding

$$\boldsymbol{\varepsilon}_S^+ = \sum_i \frac{\lambda_{Si} + |\lambda_{Si}|}{2} \mathbf{n}_{Si} \otimes \mathbf{n}_{Si}, \quad \boldsymbol{\varepsilon}_S^- = \sum_i \frac{\lambda_{Si} - |\lambda_{Si}|}{2} \mathbf{n}_{Si} \otimes \mathbf{n}_{Si} \quad (13)$$

with eigenvalues λ_{Si} and eigendirections \mathbf{n}_{Si} , while μ^S and λ^S are the partial Lamé constants. Furthermore, as the tensile part of \mathbf{T}_E^S might vanish for $\phi^S = 1$, a residual stiffness η_r^S has been included to prevent the numerical

scheme from collapsing.

Viscous pore fluid: In addition to the above, the frictional liquid stress and the extra momentum production are

$$\mathbf{T}_E^L = 2(\phi^S)^2 n^L \mu^{LR} \mathbf{D}_L, \quad \hat{\mathbf{p}}_E^L = -(1 - \phi^S)^2 \frac{(n^L)^2 \gamma^{LR}}{k^L} \mathbf{w}_L. \quad (14)$$

In these equations, μ^{LR} is the effective dynamic viscosity of the liquid, $\gamma^{LR} = \rho^{LR}|\mathbf{g}|$ is its specific weight, and k^L is the hydraulic conductivity. Apart from the liquid deformation velocity and the seepage velocity, the above equations also depend on ϕ^S . In case that ϕ^S is zero, we are in the porous-media domain. Here, \mathbf{T}_E^L vanishes and $\hat{\mathbf{p}}_E^L$ is fully dominant, meaning that we find a Darcy-flow regime. In the opposite case, when ϕ^S is one, $\hat{\mathbf{p}}_E^L$ vanishes and \mathbf{T}_E^L takes over, such that we are in the Navier-Stokes regime. Thus, we have a switch between a pore-fluid-flow and a free-flow regime. Between these regimes, there is a diffuse transition zone with $0 < \phi^S < 1$, cf. Figure 2, where both the pore fluid and the free fluid are active. To illustrate the above argumentation, one looks at the momentum balance of the pore fluid in a quasi-static case under creeping-flow conditions, and thus, with neglected inertia terms yielding

$$\mathbf{0} = \operatorname{div} [2(\phi^S)^2 n^L \mu^{LR} \mathbf{D}_L] - n^L \operatorname{grad} p + \rho^L \mathbf{g} - (1 - \phi^S)^2 \frac{(n^L)^2 \gamma^{LR}}{k^L} \mathbf{w}_L. \quad (15)$$

This equation describes the fluid flow in the transition zone and takes a reduced shape in the fractured zone with $\phi^S = 1$ and in the porous-media domain with $\phi^S = 0$:

$$\begin{aligned} \phi^S = 1 : \quad & \mathbf{0} = \operatorname{div} [2 n^L \mu^{LR} \mathbf{D}_L] - n^L \operatorname{grad} p + \rho^L \mathbf{g}, \\ \phi^S = 0 : \quad & \mathbf{0} = -n^L \operatorname{grad} p + \rho^L \mathbf{g} - \frac{(n^L)^2 \gamma^{LR}}{k^L} \mathbf{w}_L. \end{aligned} \quad (16)$$

It is seen that (16)₁ describes the Navier-Stokes equation in the reduced Stokes form, while solving (16)₂ with respect to the filter velocity $n^L \mathbf{w}_L$ yields the Darcy equation:

$$n^L \mathbf{w}_L = -\frac{k^L}{\gamma^{LR}} (\operatorname{grad} p - \rho^L \mathbf{g}) \quad (17)$$

2.1.5 Governing equations and solution procedure

The numerical treatment of porous-media problems with a single pore content is based on the mass and momentum balances of solid and fluid, where, in the case of material incompressibility, the mass balances reduce to volume balances, cf. (9)₁. Generally, one builds weak forms for the sum of the volume and momentum balances and, additionally, for the fluid momentum balance alone. This set of equation allows for solving problems, where inertia forces are integrated and where the fluid can be in the Darcy and/or the Navier-Stokes regime.

Following the above, the present problem, defined by pressing a liquid through

a porous domain given by a tiny chip with an embedded open channel numerically described by the constant history variable \mathcal{H}_0 , can easily be handled by the Finite-Element (FE) solver PANDAS¹ together with the material description in the version of Ehlers & Luo [13]. For this model, some simplifications are made and will therefore be integrated in the following set of governing weak equations. Firstly, as the chips will not be loaded by external forces or pressures, it is not necessary to use the combined momentum balance of solid and fluid. At this point, it should be noted that porous media generally need the coupling of the solid and fluid momentum balances mentioned before, as only by this procedure, the overall porous medium can decide by itself what portion of the external load is taken by the solid and what portion has to be carried by the pore content, cf. Ehlers & Wagner [16]. As this is not the case in the present consideration, where the fluid influx is prescribed while the necessary pressure has to be computed by the numerical scheme, the coupled solid-liquid momentum is reduced to the weak momentum balance of the solid alone. Therein, the inertia terms of the solid are negligible for the problems under consideration. In addition, gravitational forces have been neglected due to the tininess of the computed chips. Moreover, the thin chips are lying horizontally in the microfluidic experiments.

For the numerical solution in PANDAS, the set of primary variables $PV = \{p, \mathbf{v}_S, \mathbf{v}_L, \phi^S\}$ is used. Note that \mathbf{u}_S and \mathbf{v}_S are coupled by $\mathbf{v}_S = (\mathbf{u}_S)'_S$, such that \mathbf{u}_S can internally be found. Corresponding to the primary variables, the test functions in a Bubnov-Galerkin scheme are $\delta PV = \{\delta p, \delta \mathbf{v}_S, \delta \mathbf{v}_L, \delta \phi^S\}$. By this means, the weak formulation of the governing equations is obtained via integration over the spatial domain Ω followed by an additional definition of the necessary boundary integrals $\int_{\partial\Omega} (\cdot) da$ by use of the Gaussian integral

¹ (Porous media Adaptive Nonlinear finite-element solver based on Differential Algebraic Systems, <http://www.get-pandas.com>)

theorem, viz.:

$$\begin{aligned}
\mathcal{G}_p &= \int_{\Omega} \left(\operatorname{div} \mathbf{v}_S \delta p - n^L \mathbf{w}_L \cdot \operatorname{grad} \delta p \right) dv + \\
&\quad + \int_{\partial\Omega} \underbrace{(n^L \mathbf{w}_L \cdot \mathbf{n})}_{:= \bar{v}} \delta p da = 0, \\
\mathcal{G}_{\mathbf{v}_S} &= \int_{\Omega} \left(\mathbf{T}_E^S \cdot \operatorname{grad} \delta \mathbf{v}_S + n^S \operatorname{grad} p \cdot \delta \mathbf{v}_S + \right. \\
&\quad \left. + \hat{\mathbf{p}}_E^L \cdot \delta \mathbf{v}_S \right) dv - \int_{\partial\Omega} \underbrace{(\mathbf{T}_E^S \mathbf{n}) \cdot \delta \mathbf{v}_S}_{\bar{\mathbf{t}}_E^S = \mathbf{0}} da = 0, \\
\mathcal{G}_{\mathbf{v}_L} &= \int_{\Omega} \left(\mathbf{T}_E^L \cdot \operatorname{grad} \delta \mathbf{v}_L + n^L \operatorname{grad} p \cdot \delta \mathbf{v}_L - \right. \\
&\quad \left. - \hat{\mathbf{p}}_E^L \cdot \delta \mathbf{v}_L \right) dv - \int_{\partial\Omega} \underbrace{(\mathbf{T}_E^L \mathbf{n}) \cdot \delta \mathbf{v}_L}_{\bar{\mathbf{t}}_E^L = \mathbf{0}} da = 0, \\
\mathcal{G}_{\phi^S} &= \int_{\Omega} \left([M(\phi^S)'_S - 2(1 - \phi^S)\mathcal{H} + \frac{G_c}{\epsilon} \phi^S] \delta \phi^S + \right. \\
&\quad \left. + G_c \epsilon \operatorname{grad} \phi^S \cdot \operatorname{grad} \delta \phi^S \right) dv - \int_{\partial\Omega} G_c \epsilon \underbrace{\operatorname{grad} \phi^S \cdot \mathbf{n}}_{\equiv 0} \delta \phi^S da.
\end{aligned} \tag{18}$$

In particular, the set of coupled equations consist of the volume balance of solid and fluid multiplied by the test function δp , the quasi-static solid momentum balance multiplied by the test function $\delta \mathbf{v}_S$, the quasi-static fluid momentum balance multiplied by the test function $\delta \mathbf{v}_L$, and the phase-field evolution equation multiplied by $\delta \phi^S$. The boundary term \bar{v} in (18)₁ is later on used to induce flow in the fractured porous material. Furthermore, the present formulation additionally includes the loading boundary terms $\bar{\mathbf{t}}_E^S$ and $\bar{\mathbf{t}}_E^L$ which are, however, not applied in the context of this study. This means that solid deformations are only triggered by the pore-fluid flow. Note in passing that the restriction $\operatorname{grad} \phi^S \cdot \mathbf{n} \equiv 0$ follows from the evaluation of the entropy inequality (10). For the numerical solution, the set of equations is discretised in space using a Taylor-Hood formulation with quadratic approximation functions for \mathbf{v}_S and \mathbf{v}_L and linear approximation functions for p and ϕ^S to fulfil the inf-sup criterion for a stable computation, cf. Fortin & Brezzi [19]. Moreover, the time discretisation is realised by an implicit finite-difference scheme (backward Euler) leading to a monolithic solution of the numerical problem.

2.2 Discussion of the length-scale parameter

As stated earlier, the length-scale parameter ϵ is of particular importance in phase-field models. However, there are different ways to interpret and use this parameter. For fractures in single-phasic solid materials, it could be stated that ϵ should be chosen as small as possible to approximate a sharp fracture as tightly as possible. This, however, might not be the case for the fluid-saturated material studied in this contribution, since a transition between a faster flow in the fracture and a slower flow in the surrounding porous material is occurring. The existence of a transition zone is reported in Beaver & Joseph [3] for flow over a fully saturated porous material. In this case, the length-scale parameter needs to be chosen small enough to represent the fracture geometry but on the other hand large enough to capture this transition region. For the spatial discretisation, the mesh size for the finite-element simulations needs to be in agreement with the chosen transition zone, as was recommended for example by Miehe et al. [32]. This set of thoughts gives rise to the general idea to find physically feasible values of ϵ based on the natural properties of the materials or processes in agreement with the chosen discretisation. In the considered case of modelling fractures in a fully saturated solid material, the length-scale parameter ϵ in (7) determines the transition length between two limiting states of the solid body, fully broken and intact. To study the flow interaction between the fully broken and intact region we will later (Section 3.4) use a microfluidic chip which contains a regular porous structure with repeating unit cells, as shown in Figure 3 (orange square), and a rectangular channel in the middle as a representative replacement model. A real-world analogy would be an open, single fracture in a saturated aquifer. However, for the general discussion we stay in the frame of the simple (academic) example of the microfluidic device in Figure 3. Here, we assume that the channel walls represent rough fracture surfaces, where an expected fracture path can be anticipated on the repeating unit-cell boundaries, as shown in Figure 4 in red. Hence, inspired by Chabaan et al. [7], the length-scale parameter needs to be

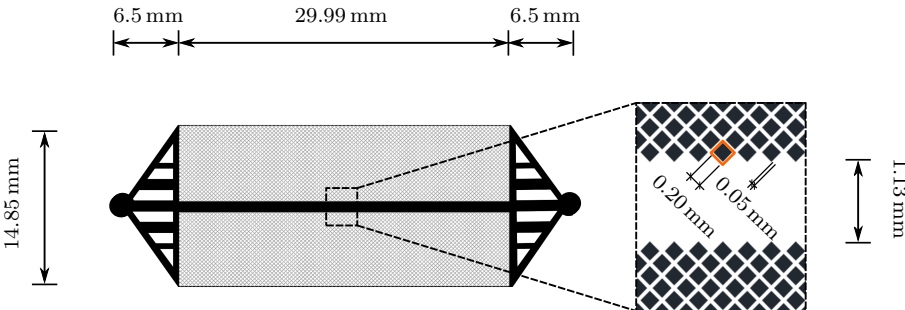


Fig. 3: Design and geometry of the considered microfluidic chip.

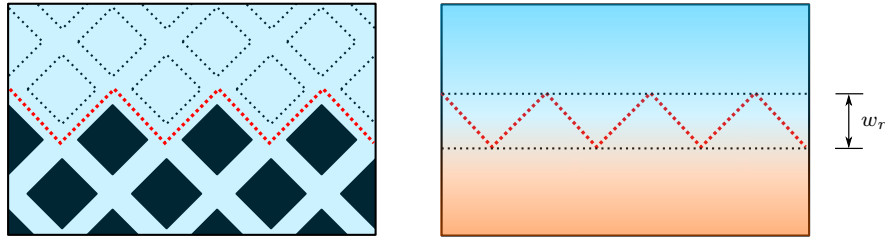


Fig. 4: Fracture approximation for the investigated microfluidic chips.

selected such that the transition zone's width x corresponds to a relative width w_r between local minima and maxima (amplitude) of the red-coloured fracture path, i.e. one half of the unit cell's diagonal, cf. Figure 3. To estimate the corresponding length-scale parameter ϵ for this pore structure, Equation (7) is rearranged as follows

$$\epsilon = -\frac{|x|}{\ln(\phi^S)} = -\frac{w_r}{\ln(\phi^S)} = -\frac{\frac{250\mu\text{m}}{\sqrt{2}}}{\ln(0.01)} \approx 40\mu\text{m}. \quad (19)$$

Since we are interested in the value of ϵ which leads to the diffuse transition width, the phase-field variable is chosen small such that the material beyond the transition domain is to 99 % in its intact state. This limit value is chosen analogously to considerations of (asymptotic) boundary-layer phenomena. The obtained value of $\epsilon \approx 40\mu\text{m}$ is used for the corresponding numerical simulations of the microfluidic samples later on.

However, the advantage of the proposed approach is that it can also be transferred to fracture surfaces in real porous rocks. In Mlynarczuk [34], the fracture surface of various rock samples was prepared using the Brazilian fracturing test and subsequently scanned using laser profilometry. The dataset was evaluated by an algorithm determining the relative height between local minima and maxima, which corresponds to the minimum and maximum of the fracture path described above. This allows to calculate values as estimates for the length-scale parameter ϵ for the different rock types analysed in the mentioned article [34], cf. Table 1. For granular materials, such as sandstone, it is apparent that roughly doubling the grain size doubles the relative width, which further implies a dependency between fracture-path amplitude and grain size.

As a remark, this simple approach only considers geometric properties of the microscopic pore structure to describe the transition region. Therefore, the idea can be used for macroscopic fracturing problems, regardless of considering single-phasic or saturated multiphasic solid materials. This may avoid an arbitrary choice of the length-scale parameter in many phase-field simulations.

rock type	grain size [μm]	width w_r [μm]	estimated ϵ [μm]
Wisniówka Sandstone	80 – 200	70	15
Tumlin Sandstone	40 – 400	148	32
Redziny dolomite	100 – 300	120	26
Laskowa Góra dolomite	200 – 600	101	22
Limestone	30 – 50	61	13

Table 1: Estimated values for ϵ for fractured rock samples based on the experimental investigations presented by Mlynarczuk [34].

3 General numerical study

3.1 Problem setup for the general study

The general numerical study presented in this section examines the flow behaviour in thin porous plates (chips) under different flow boundary conditions. These conditions of the initial-boundary-value problem (IBVP) are motivated by the potential application of modelling microfluidic chips or similar technical devices with relatively low flow velocities, cf. Section 4. In Figure 5, a top view of the geometry with corresponding boundary conditions is sketched. In particular, the plate has a rectangular base area of depth $d = 200 \mu\text{m}$ in the \mathbf{e}_3 -direction perpendicular to the top view. In the centre of the plate, there is a channel ($l/w_f/d = 40/1/0.2$ [mm]) running through the chip in \mathbf{e}_1 -direction from one side to the other for the complete depth d as a fully open fracture modelled by use of the phase-field approach via the assignment of \mathcal{H} from (8). This channel has two opposing porous boundaries (interfaces) that allow for liquid mass exchange between the coupled flow regimes. At the top and bottom of the porous plate, a no-slip (Dirichlet) boundary condition $\mathbf{v}_L = \mathbf{0}$

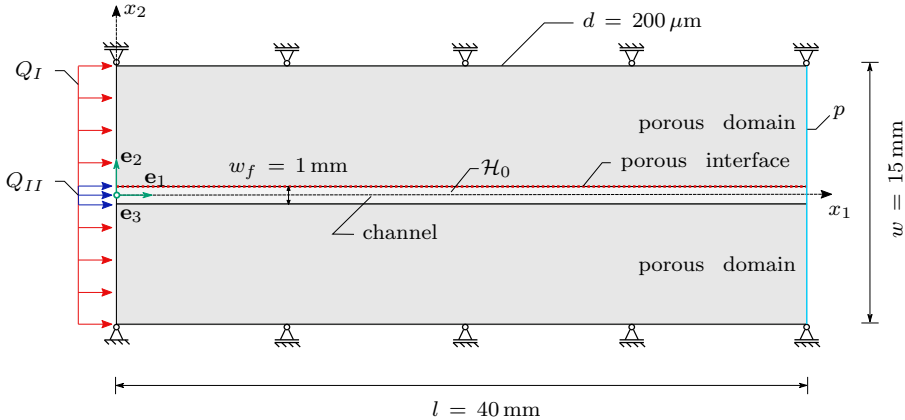


Fig. 5: Sketch (top view) of the problem setup for the general study.

λ^S	=	1.211×10^{11}	[Pa]	: 1st Lamé parameter of the solid skeleton
μ^S	=	8.077×10^{10}	[Pa]	: 2nd Lamé parameter of the solid skeleton
G_c	=	0.1	[Pa m]	: Crack resistance
ϵ	=	40×10^{-6}	[m]	: Length-scale parameter
η_r^S	=	1.0×10^{-3}	[·]	: Residual stiffness
μ^{LR}	=	1.002×10^{-3}	[Pas]	: Dynamic viscosity of the pore liquid
ρ^{SR}	=	3×10^3	[kg/m³]	: Real density of the solid skeleton
ρ^{LR}	=	1×10^3	[kg/m³]	: Real density of the pore liquid
k^L	=	$1 \times 10^{-3} - 1 \times 10^{-6}$	[m/s]	: Hydraulic conductivity

Table 2: Material parameters for the general study

is applied, whereas the boundaries perpendicular to \mathbf{e}_2 are featuring slip. The solid skeleton of the porous plate is considered sufficiently rigid and supported to endure the forces imposed by the liquid-flux boundary conditions on the left edge. Furthermore, the pore pressure p , here taken as the excess pore pressure, is set to zero along the entire right edge. The plate is exposed to a flux $Q_i = \bar{v}A_i$ from the left edge, either across the entire cross section A_I (Case I) denoted as Q_I in Figure 5 or only on the channel cross section A_{II} (Case II), respectively denoted as Q_{II} .

The consideration of these two distinct cases allows for the isolation and discussion of effects arising from the geometry of the inflow cross section, cf. Section 3.2. In Case I, the uniformly distributed flow field reaches the porous domain with a certain hydraulic conductivity and the free-flow channel which does not hinder the flow. This scenario may represent the flow in a geological formation containing an open fracture. In contrast, Case II can be discussed as channel flow with porous boundaries as a typical usecase in technical applications, e.g. geothermal energy harvests. Under realistic conditions, there would be no solid component present in the free-flow channel, i.e. $n^S = 0.0$. However, this would cause the global system of equations used in this single-domain approach to collapse, as individual equations would be omitted in certain regions. Therefore, a very small initial solid fraction of $n_0^S = 0.01$ is chosen in the channel, still providing sufficient accuracy for the considered issues. Furthermore, the initial solid fraction of the surrounding porous domain is set to $n_0^S = 0.57$. The material parameters for this general study are given in Table 2, where the length-scale parameter is chosen as discussed in Section 2.2. The mesh of the model consists in total of 4 224 three-dimensional hexahedral elements. It is refined in the vicinity of the left boundary to resolve the entrance effects studied in Section 3.3. On the same basis, the width of the channel is meshed finely with 16 elements to meaningfully resolve the arising velocity profile. The depth of the plate is meshed using four elements in thickness direction, which is considered enough for the purpose of this study, since there is no significant flow in \mathbf{e}_3 direction. In order to resolve the transition of

the phase field properly, the mesh in the transition region is chosen according to the considerations given in Miehe et al. [32].

3.2 Flow in thin fractured porous plates

This section discusses the solutions of the previously described general study, cf. Section 3.1, under the consideration of different hydraulic conductivities of the porous region with an applied flux of $Q_I = Q_{II} = 0.1 \text{ ml/min}$. In particular, the focus is here on the interaction between the porous region and the free flow channel. Figure 6 shows the streamlines for both cases using a hydraulic conductivity of $k^L = 10^{-4} \text{ m/s}$. It is apparent that in Case I the liquid percolates from the porous domain towards the channel leading to high velocities around point A. In contrast, the liquid is pushed from the channel into the surrounding porous material in Case II. Note that the in- or outflow of the channel is evaluated at the upper porous interface marked as a dotted red line in Figure 5.

Considering Case I, the liquid is applied as a uniform velocity field and therefore directly hits either the porous material which hinders the flow and, at the same time, the free flow channel which provides less resistance. While study-

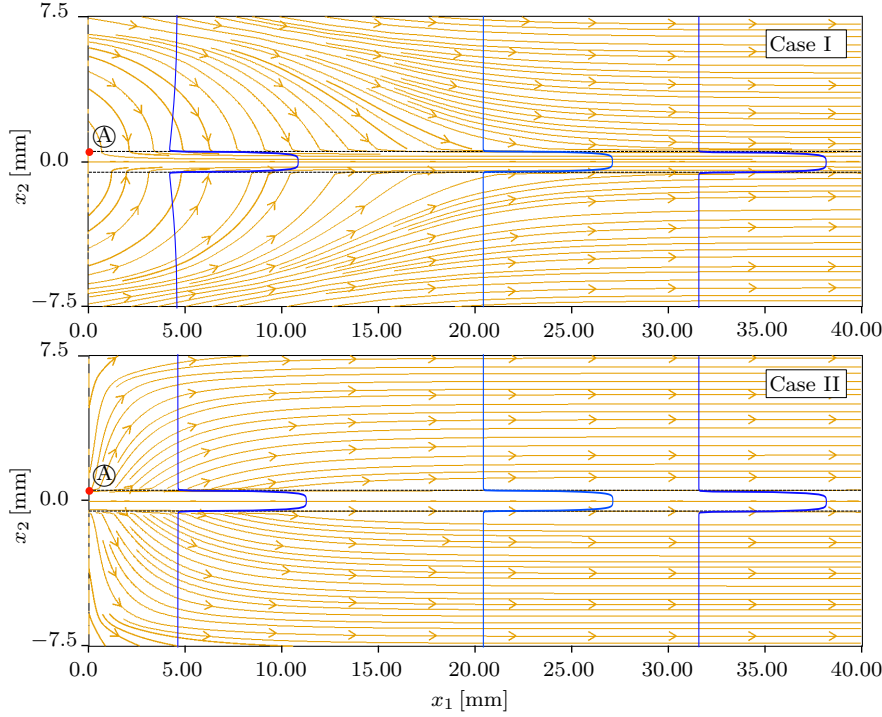


Fig. 6: Streamlines for Case I (top) and Case II (bottom) with global velocity profiles at distinct locations.

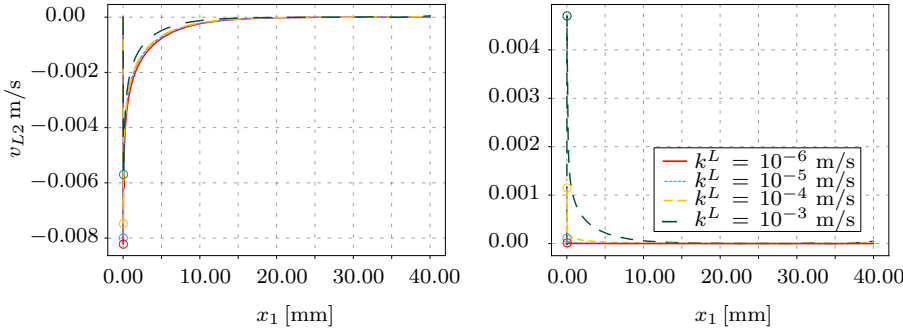


Fig. 7: Vertical velocity component over the porous interface over the length of the domain for Case I (left) and Case II (right).

ing the effects of different hydraulic-conductivity values, it was found for lower values that the vertical velocity components near the inlet were higher than for larger values. Figure 7 (left) shows the vertical velocity over the diffuse interface plotted over the length of the model. Furthermore, considering the general flow development in the channel, Figure 8 shows the axial velocity in the centre, plotted over the length of the model. As is seen from Figure 7 (left), the porous material feeds the channel until an equilibrium between the domains is reached and thus, the velocities stay constant until the influence of the right boundary takes over. Moreover, higher axial velocities are observed for lower hydraulic conductivities, which makes sense since the liquid's mass is conserved. Generally, the liquid's cross-flow behaviour to reach an equilibrium between the domains strongly depends on the hydraulic conductivity. For larger values, the liquid is able to percolate in the basic direction of flow, whereas lower values lead to a distinct flux towards the channel, in particular in the vicinity of the inlet region. This finding coincides with a certain "well-effect" observed from the global velocity profile near the inlet, cf. the blue line in Figure 6 (top), which vanishes further downstream. In contrast to Case I, the flux for Case II is exclusively applied to the channel's left boundary which mimics channel flow within porous boundaries. As already implied, the channel loses liquid mass to the porous material depending on the hydraulic conductivity until an equilibrium state is reached, cf. Figure 8 (right). For low values, nearly no interaction between the domains is observed whereas increasing the value leads to significant distribution of liquid mass across the two domains. This is additionally reflected in Figure 7 (right). Studying the global velocity profile close to the inlet does not show a significant effect at the diffuse transition region for the displayed hydraulic conductivity. However, the large vertical flux for larger values of hydraulic conductivity displayed in Figure 7 indicates that, close to the inlet, more liquid mass is present in the permeable transition zone between the domains. To quantify the occurring mass exchange over the permeable interface, the velocities are integrated over the entire length of the upper porous interface marked as a dotted, red line in

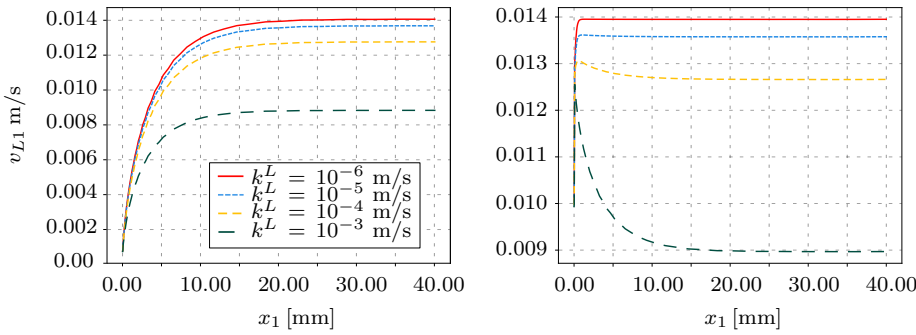


Fig. 8: Centre-line velocity along the x_1 -axis in the channel over the length of the sample for Case I (left) and Case II (right).

Figure 5. The resulting fluxes are given in Table 3 for four different hydraulic conductivities. It is observed that for Case II, and especially for low hydraulic conductivities, the interaction between both domains is small enough to argue that there is mainly flow occurring in the channel. These findings can be very useful for the determination of, for example, initial pumping rates for the planning of injection-production systems such as geothermal energy plants.

k^L [m/s]	Case I		Case II	
	Q [ml/min]	Q [ml/min]	Q [ml/min]	Q [ml/min]
10^{-6}	-0.0822	0.0006		
10^{-5}	-0.0473	0.0014		
10^{-4}	-0.0417	0.0036		
10^{-3}	-0.0301	0.0155		

Table 3: Fluxes across the entire interface between the porous domain and the channel for different hydraulic conductivities, evaluated at the upper porous interface marked as dotted, red line in Figure 5.

3.3 Velocity profile inversion phenomena

Looking at the local flow behaviour in the channel, interesting effects are observed in the entrance region concerning the development of the liquid velocity profile. The entrance region is defined as the region where the effects are observed whereas the development region is referred to as the length required for the flow to fully develop, in this study at approximately $x_1 > 20$ mm, cf. Figure 6. During the investigation of the developing velocity profiles along the length of the model it has been found that over a certain entrance length

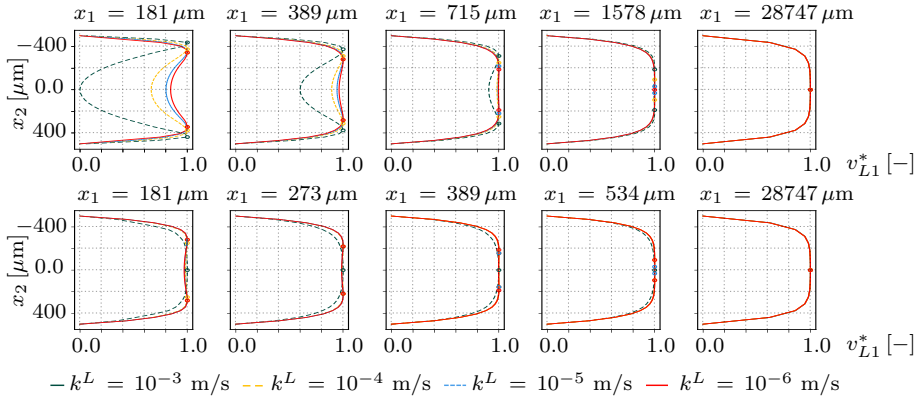


Fig. 9: Development of the normalised velocity v_{L1}^* showing the inversion phenomena for Case I (upper row) and Case II (lower row) along the channel width for different hydraulic conductivities.

from the inlet, off-centre velocity peaks develop near the porous interfaces. The velocity peaks converge towards the centre line of the channel as the flow develops, cf. Figure 9. Such velocity peaks were observed experimentally by Reci et al. [35] and given the name velocity profile inversion. The reason of this inversion phenomenon is thoroughly discussed for different inlet conditions and varying fluxes in pipe flow, cf. Haustein & Kashi [21]. It has been shown that not only the inlet geometry has a huge impact on the inversion but also effects due to a vertical flow in the development region. As long as vertical velocities are included in the modelling approach, their presence is intuitively explained by mass conservation, included in the liquid mass balance for regimes with constant porosity n^L :

$$\operatorname{div} \mathbf{v}_L = \frac{\partial v_1}{\partial x_1} + \frac{\partial v_2}{\partial x_2} + \frac{\partial v_3}{\partial x_3} = 0. \quad (20)$$

In the development region, the spatial change of the axial velocity $\partial v_1 / \partial x_1$ is not equal to zero which, as a result of spreading liquid into the porous domain, must lead to non-zero values for the vertical velocity components. Additionally, geometrical effects, such as sharp narrowing of a channel, lead to higher velocities at the channel walls close to the inlet. In line with those findings, the same observations were made by Lobo & Chatterjee [31] considering rectangular channels with a narrowing inlet plenum.

In this contribution, a specific focus is placed on the influence of flux inwards or outwards of the channel. Obviously, the permeable porous interfaces (boundaries) have a considerable effect on the inversion phenomena. Figure 9 shows the normalised velocity profiles $v_{L1}^*(x_2)$ at different cross sections through the channel measured from the inlet at $x_1 = 0$. Note that the shown normalised velocity in the channel only represents a local section of the whole model domain. To make the inversion effect better visible, a min-max normalisation via $v_{L1}^*(x_2) = (v_{L1} - v_{L1\min}) / (v_{L1\max} - v_{L1\min})$ was used. Generally, the velocity

peaks appear near the porous channel walls and, in line with the observations in the above mentioned literature, develop towards the centre of the channel and decrease in magnitude as the flow evolves. Furthermore, it is observed that for Case I, where liquid is sucked into the channel, the velocity overshoots are more pronounced and the profile takes considerably longer to lose the velocity peaks. In contrast to Case II, again referring to Lobo & Chatterjee [31], the abrupt restriction of area available for flow additionally increases the effect, since larger vertical velocities arise at the inlet, cf. Figure 7. In Figure 10, the maximum velocity peaks are quantified (as a percentage) for both cases via a comparison to the axial velocity in the considered cross section over the channel via $(v_{1\max} - v_{1\text{centre}})/v_{1\text{centre}}$. It is observed for both cases that the magnitude of the peaks decrease with an increasing distance from the inlet. However, the overshoots are largest for the largest hydraulic conductivity for

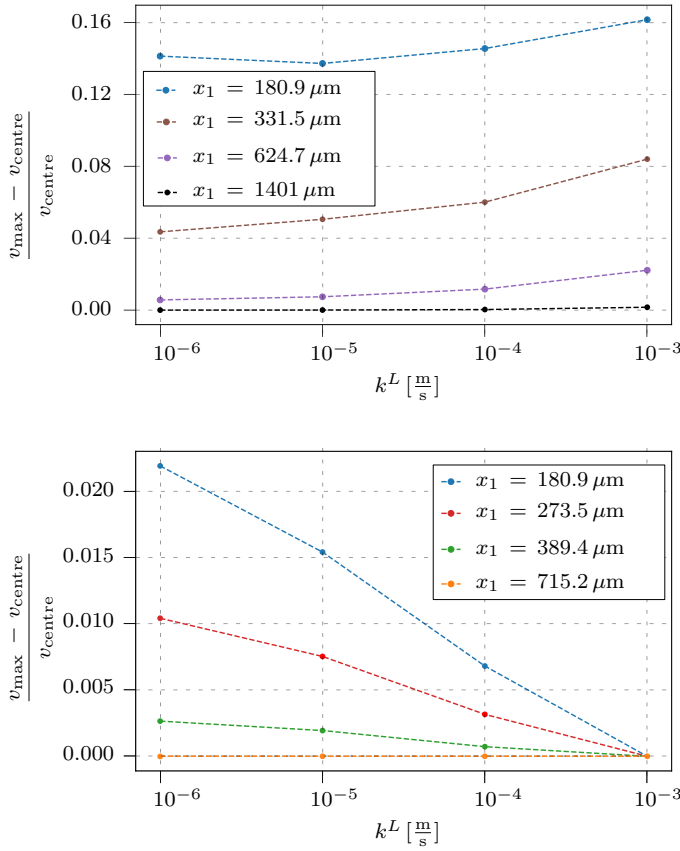


Fig. 10: Velocity overshoots at the porous boundary at different cross sections given for different hydraulic conductivities for Case I (top) and Case II (bottom).

Case I, whereas the opposite is observed for Case II. Considering Case I, this outcome is also reflected in the large vertical velocities at the corner point A, referred to in Figure 6, for small values of hydraulic conductivities. To conclude the outcomes, the fact that the inversion phenomenon is increased for fluxes into the channel and is relaxed for fluxes out of the channel is particularly notable. Furthermore, it is observed that the appearance of the velocity inversion is strongly connected to arising vertical velocities, which in the considered study depend on the applied boundary conditions and hydraulic conductivities of the porous domain.

3.4 Numerical preparatory studies of microfluidic chips

In the preceding general studies, we presented the ability of the TPM phase-field approach to model complex, coupled flow phenomena. To proceed to a practical application, we present in the following a numerical study of microfluidic chips in an (iterative) numerical-experimental context with the aim to confirm the theoretical ideas discussed in Section 2.2 for the flow behaviour over rough porous walls and verify the overall model. In particular, two types of mi-

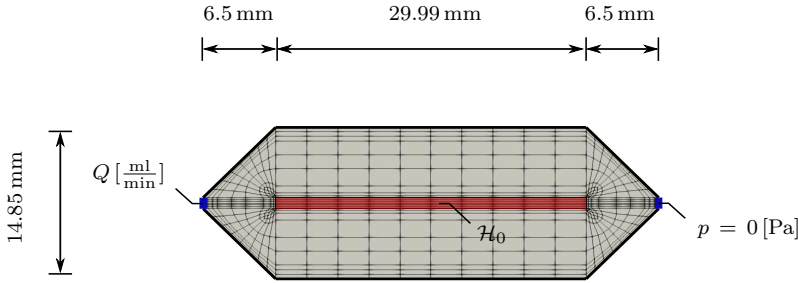


Fig. 11: Corresponding numerical model of a microfluidic chip with embedded fracture (rectangular channel).

crofluidic chips have been investigated experimentaly, uniform porous samples to estimate the base hydraulic conductivity of the porous domain, and samples with an embedded rectangular channel, in analogy to Figure 3, for the study of the interaction between free flow and porous-media flow. The porous domain of both chips have a solid volume fraction of $n^S = 0.61$ and a maximum throat size of the pores of $50 \mu\text{m}$. Furthermore, the chips are produced with an inlet and outlet domain, which is technically necessary to provide an equally distributed flow throughout the porous domain under study. In the numerical model shown in Figure 11, the in- and outlet domains are macroscopically considered as a porous material with a solid volume fraction of $n_i^S = 0.40$ (geometrically evaluated from the structural composition) and the hydraulic conductivity k_i^L . The hydraulic conductivity of the porous domain in the chip is denoted as k_p^L . The hydraulic boundary conditions are applied according to

Figure 11 with a flux $Q = \bar{v}A$ on the left edge and a zero (excess) pressure condition at the right edge. To prevent deformations of the outer sides, the chip is supported by zero displacement boundary conditions. Regarding liquid flow, no-slip boundary conditions are applied at all outer surfaces of the sample. The assignment of the fracture via \mathcal{H}_0 is conducted as described in Section 3.1. Furthermore, to accurately model the behaviour of the chips, the Lamé parameters of the solid Poly-Di-Methyl-Siloxane (PDMS) body are chosen according to Johnston et al. [25], see Table 4 for the corresponding material parameters. The total number of elements for meshing the microfluidic chips is 4 336 and as in Section 2 similar choices regarding the refinement are made, cf. Figure 11. By means of the mentioned iterative numerical-experimental

λ^S	=	3.41×10^8	[Pa]	: 1st Lamé parameter of the solid skeleton
μ^S	=	6.8×10^5	[Pa]	: 2nd Lamé parameter of the solid skeleton
G_c	=	0.1	[Pa m]	: Crack resistance
ϵ	=	40×10^{-6}	[m]	: Length-scale parameter
η_r^S	=	1.0×10^{-3}	[·]	: Residual stiffness
μ^{LR}	=	1.002×10^{-3}	[Pa s]	: Dynamic viscosity of the pore liquid
ρ^{SR}	=	965	[kg/m ³]	: Real density of the solid skeleton
ρ^{LR}	=	1000	[kg/m ³]	: Real density of the pore liquid

Table 4: Material parameters for the microfluidic PDMS chip.

approach, a preparatory numerical study is conducted to evaluate the influence of the thickness of the microfluidic chips. In Figure 12, the results from a numerical study of the ratio of the pressure gradients $\text{grad } p_f$ and $\text{grad } p_p$ for fractured and non-fractured porous models, respectively, are shown for varying model depths d . Therein, one can see clearly that, as expected for a decreasing thickness, the pressure gradient of the fractured model is getting closer to the pressure gradient of the non-fractured model. This is caused by the circumstance that the thickness is dominating the hydraulic conductivity by the fact that top and bottom of the chip exhibits no-slip boundary conditions. As a result of a decreasing chip depth, hydraulic conductivity of the porous domain without fracture shrinks faster than the conductivity of the fractured domain, what naturally affects the mean conductivity of the chips. The influence of the channel (fracture) disappears when the depth of the microfluidic chips (and the depth of the channel) tends towards the throat size of 50 μm in the porous domain, cf. Figure 12. Moreover, from the ratios presented in Figure 12, it can be concluded that for a thickness between 200 – 400 μm a pronounced drop in the pressure gradient ratio occurs, while for ratios greater than 400 μm , the curve flattens. This indicates the need to produce higher microfluidic chips since a standard thickness is around 100 μm . In general, it can be concluded that accounting in microfluidic studies for the influence of the model depth while studying the global hydraulic resistance of a microfluidic chip (e.g. for

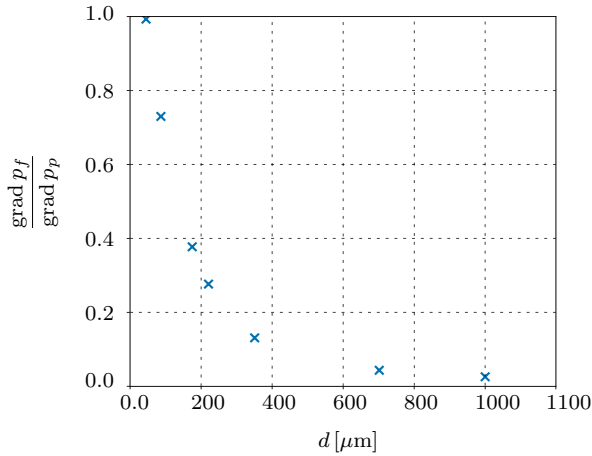


Fig. 12: Numerical results for the comparison of the pressure gradients in microfluidic devices with and without a fracture for different chip depths d .

the estimation of hydraulic conductivities) is of great importance. Obviously, this accounts for both, intact and fractured porous samples. Certainly, the ideal way to cope with this is a three-dimensional simulation, which can naturally take into account all boundary influences. However, if computing time or model limitations require a two-dimensional simulation, the three-dimensional effects need to be considered in an adequate manner for a dimensionally reduced formulation, cf., e.g., the works of Flekkøy et al. [17], Weishaupt et al. [48] or Krach et al. [29].

A further aim of the preparatory study is to study the role of solid deformations. Therefore, the simulated solid displacement field $|\mathbf{u}_S|$ is evaluated for a maximum applied flux of 2.5 [ml/min], which corresponds to a maximum applied pressure of approximately 25 mbar in the experiments, cf. Section 4.2. The simulation results are shown in Figure 13. Compared to the minimum pore size of 50 μm in the porous domain, cf. Figure 3, the deformations are very small with a maximum value of approximately $0.9 \times 10^{-3} \mu\text{m}$ in the porous domain. Therefore, it can be stated that solid deformations are not relevant

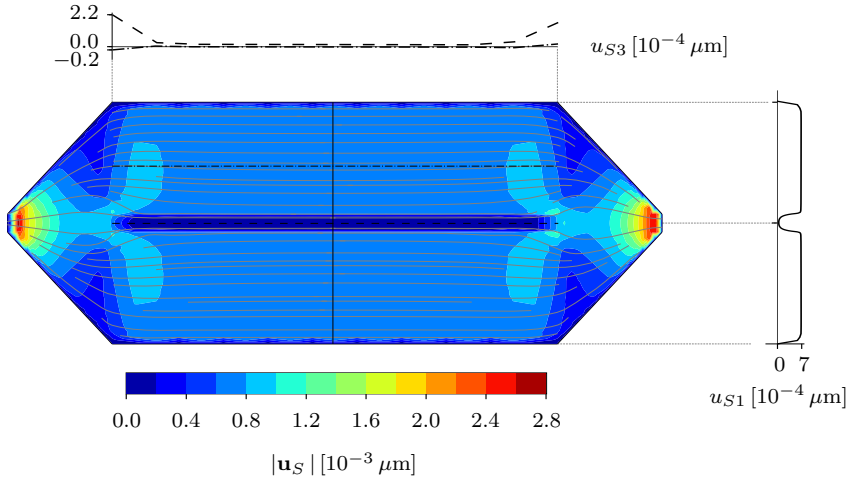


Fig. 13: Displacement field and liquid streamlines within the microfluidic chip.

for the flow processes in this study. This is also seen, implicitly, in the obtained linear flux-pressure relationship in Figure 15. Nevertheless, these simulations results show the capability of the TPM-phase-field model to predict solid displacements. The extracted line plot of the solid displacements in the e_1 -direction shows the basic deformation behaviour. The resistance and therefore the resulting solid deformation, is much higher in the porous region than in the free-flow channel due to the absence of solid material there. In this regard, the streamlines in Figure 13 follow the slightly higher displacements in the regions where the liquid flows into and out of the channel indicating higher velocities. Finally, one can directly relate the flow behaviour in the simulated microfluidic device to the flow behaviour in Case I of the general study while comparing the streamlines in Figure 6 and Figure 13.

In conclusion, the performed general numerical simulations in Section 3 delivered useful knowledge for the design and the setup of the following experiments on microfluidic chips in Section 4. Overall, we have drawn two conclusions from this. Firstly, we need the production of microfluidic samples with a reasonable height and, secondly, we were strongly encouraged in our approach to carry out fully three-dimensional simulations promising greater success than simplified two-dimensional approaches.

4 Microfluidic experiments and their simulation

In the pursued combined numerical-experimental strategy we build on tailored microfluidic experiments, investigated at the Porous Media Lab (PML) of the University of Stuttgart. Obviously, a successful combination of experiments and simulations is only possible through a very close collaboration between

researchers from both fields. As a result, an iterative process naturally arises in which both areas can benefit greatly.

4.1 Manufacturing process and properties of microfluidic chips

The microfluidic chips used in this work were made of Poly-Di-Methyl-Siloxane (PDMS). PDMS is a naturally hydrophobic, silicone-based polymer known for its flexibility, transparency, and biocompatibility. It is chemically inert, non-toxic and highly resistant to temperature variations. The process of producing a microfluidic chip is described in detail in Xia & Whitesides [49]. In short, PDMS micromodels are created using a combination of soft lithography and optical lithography. First, a silicon wafer is coated with a photosensitive polymer (photoresist). Using optical lithography, ultraviolet (UV) light is shined through a mask to pattern specific areas, creating a mold with raised features that correspond to the desired microstructures. A mixture of an elastomer base and a curing agent of PDMS is then poured over the patterned silicon mold. After curing, the PDMS layer is peeled off, capturing the negative of the micro-patterned structure. This PDMS slab is bonded to glass or another PDMS layer to create a sealed microfluidic channel network that can be used for experiments. For the needs of our experiments, a mask was created bearing the exact structure as displayed in Figure 3 and Figure 14 (left) to manufacture our PDMS replicas.

4.2 Basic experimental setup

Two independent experimental setups are investigated, targeting different sets of measurements. First, the measurement of the hydraulic conductivity and, second, the determination of the velocity field for a variety of flux boundary conditions. For the estimation of the hydraulic conductivity of the microfluidic chip, a Cetoni[©] mid-pressure syringe pump and an MPS0 Elveflow[©] pressure sensor were used. The syringe pump was used with a 2.5 ml glass syringe and was controlled by a computer via QmixElements (Cetoni[©]) for the application of various flow rates at the inlet of the microfluidic chip. The MPS0 sensor, capable of accurately recording pressures of up to 70 mbar, was also connected to the computer and controlled via QmixElements, for the logging of the pressure values at a rate of 10 Hz. The experimental setup presented here is similar to the one used in Wagner et al. [45], with the only difference that no second sensor was used and the outlet pressure was taken as atmospheric.

The experiment starts with the micromodel being completely saturated with ethanol, in a way that air was completely expelled from the pore space. Then, water was introduced into the flow network for at least 10 pore volumes. As soon as ethanol was out of the pore space, as a result of the displacement process by the water, the flow was stopped and the inlet pressure was measured. We confirmed that the sensor readout corresponded to the hydrostatic

pressure induced by the connecting tube at the inlet. This pressure was used as the calibration point for all further measurements of the same experimental cycle. Then, the boundary flux was increased to a certain value. As soon as the pressure reached a steady state, the flux was again increased further. Several incremental steps were taken, and we recorded both the actual flux value, and the corresponding pressures. The slope of the fitted line can then be used to estimate the hydraulic conductivity of the microfluidic model via Darcy's law. Furthermore, the experiment would stop if the measured pressure would exceed 25 mbar since above this value the pore space of the microfluidic chip expands significantly. As a consequence, the behaviour between flux and pressure is no longer linear as prescribed by Darcy's law and therefore not suitable anymore for the determination of the hydraulic conductivities. Proceeding, equivalent measurements with the same fluxes were done with a structure bearing with only the inlet and outlet of the microchip to obtain the corresponding pressures. Therefore, a subsequent calculation of the pressure drop occurring only in the porous medium is possible, excluding the influence of the inlet and the outlet, as presented in Section 4.3.1. Since the model with the porous medium and the porous medium including the fracture have the same inlet and outlet design we only needed to measure the pressure drop for the corresponding fluxes for the inlet and outlet once.

For the identification of the velocity field inside the fracture and the porous medium we used Particle Image Velocimetry (PIV), cf. Adrian [1]. PIV is an optical technique used to measure the velocity and flow patterns of fluids. It works by seeding a fluid with small tracer particles and illuminating them with high intensity light. High-speed or dual shutter cameras capture images of the particles at different time intervals. The velocity fields can be calculated by analysing the displacement of particle groups between frames. The experimental setup for the determination of the velocity field was similar to the one used in Dastjerdi et al. [10]. A Cetoni[©] mid-pressure syringe pump and a 2.5 ml syringe were used for the application of the boundary flux conditions at the inlet of the microfluidic chip. The imaging setup is similar to the ones used in Dastjerdi et al. [10] and Karadimitriou et al. [26] with some modifications. The process was visualised with an Cyclone-5-700 Optronis GmbH monochrome camera. The camera was capable of recording 5 megapixel (Mpx) images at a frame rate of 693 frames per second (fps). After binning to an area of interest of $256 \times 8 \text{ px}^2$ the acquisition frame rate could go as high as 95K fps. Given the volume of information per second, a frame grabber is needed, and for this purpose an Euresys Coaxlink Quad CXP-12 frame grabber was used. The PCI Express frame grabber was installed on a PC with an Intel[©] i9 processor and 128 GB of RAM. The images were recorded directly to the RAM, since the recording was too fast for the M.2 SSD hard disk drive to cope with. Recording and control of the camera took place with the use of StreamPix 9 from NorPix[©]. For the visualisation of flow and the identification of the velocity field, mono-disperse, polystyrene particles (with a mean diameter of 3.97 microns, a standard deviation of 0.06 microns and density of 1040 kg/m³, from microparticles GmbH) were used as the tracers. The flow

was illuminated with a Chrolis C1 LED source at a wavelength of 565 nm. The synergy between the light source and StreamPix allowed us to reduce the camera exposure time and increase the light intensity, so that the camera shutter remained open for a shorter time and sharp images of the particles were obtained at all times. The images were taken with a spatial resolution of 1 micron per pixel and a maximum temporal resolution of 693 frames per second. This meant that an image was captured every 1.4 milliseconds.

4.3 Experimental results and their adaption for the numerical model

4.3.1 Experimentally determined hydraulic conductivities of microfluidic chips

Since the hydraulic conductivity k_T^L of the complete microfluidic chip, cf. Figure 14 (left), as well as the hydraulic conductivity k_i^L for two directly connected identical inlet and outlet domains, cf. Figure 14 (right), were determined experimentally, the hydraulic conductivity for the porous domain k_p^L can be calculated in terms of a serial connection using the known pressure differences Δp_j . Therefore, applying Darcy's law (17) with neglected gravitational forces,

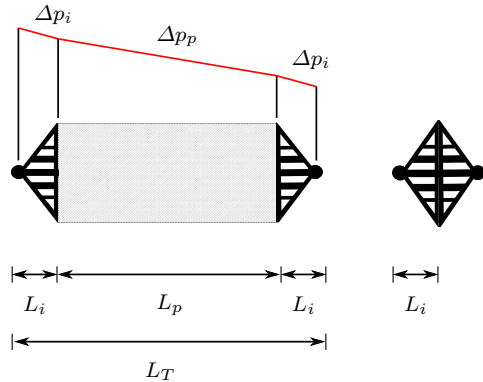


Fig. 14: Microfluidic chip (left) and connected inlet and outlet (right).

the following relation is found

$$Q_j = A_j \frac{k_j^L}{\gamma_{LR}} \text{grad } p_j, \quad \text{where} \quad \text{grad } p_j = \frac{\Delta p_j}{L_j} \quad \text{and} \quad j = \{T, i, p\}. \quad (21)$$

Therein, Q_j are the volume fluxes over the cross sectional areas A_j and L_j the length of the considered sections, cf. Figure 14. After rearranging (21) with respect to the pressure differences Δp_j and writing the total pressure difference Δp_T in terms of the sum of all pressure differences $\Delta p_p + 2\Delta p_i$, an expression

for k_p^L is found as

$$k_p^L = \frac{L_p}{\left(\frac{L_T}{k_T^L} - \frac{2L_i}{k_i^L} \right)}. \quad (22)$$

Note that the volume fluxes Q_j cancel in the above equation due to continuity ($Q_T = Q_i = Q_p$). Furthermore, the cross sectional areas A_j are assumed to be constant in \mathbf{e}_1 -direction (length direction) leading to linearity in the section-wise pressure drop. The results of the experimentally measured hydraulic conductivities and the calculated hydraulic conductivity k_p^L for the intact (unfractured) chip are given below in Table 5.

k_T^L [m/s]	k_i^L [m/s]	k_p^L [m/s]
3.237×10^{-3}	8.721×10^{-3}	2.543×10^{-3}

Table 5: Experimentally determined hydraulic conductivities of the intact chip

The experimentally determined hydraulic conductivity k_p^L for the intact (unfractured) chip is used as a base material parameter for the numerical simulation of the microfluidic chip with the embedded fracture (rectangular channel). According to the geometry of the microfluidic model shown in Figure 3, a corresponding numerical model with a depth of $190 \mu\text{m}$ is considered as shown in Figure 11. In the experiments, only the pressure at the inlet and the atmospheric pressure at the outlet are known. Therefore, the simulated

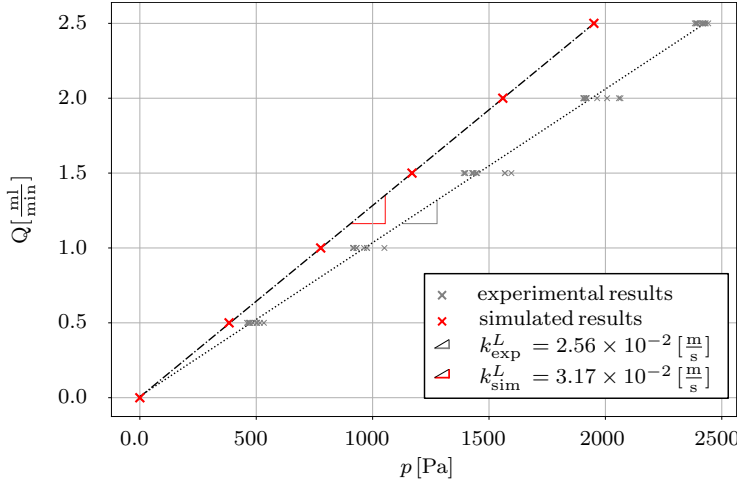


Fig. 15: Comparison of simulated and experimental inlet pressures for the microfluidic chip with embedded channel.

and experimentally measured inlet pressures of the microfluidic chip containing the channel are presented for a range of fluxes Q in Figure 15, showing a very good agreement in their general trends. This suggests that the model accurately captures the physical key processes and shows the predictive capability of the simulations. For the experiments, a linear fitting resulted in a coefficient of determination R^2 of 0.99 and above. The resulting slope, or using the linear flux-pressure relationship given by Darcy's law, yields the global hydraulic conductivity, which is in the same order of magnitude but differs by approximately 19 percent. This slight deviation can be caused by the fact that several real world properties of our experimental setting, as for example irregularities in surface roughness or local deviations of the depth of the microchip, are very difficult to be identified and, thus, cannot easily be considered in the numerical model. Furthermore, using multiple experimental setups to determine and compare the hydraulic conductivities for the numerical model add onto this uncertainty. The later statement strongly motivates the use of different experimental designs which feature pressure measurements at discrete locations in the microchip, such that the in- and outlet domains can be completely neglected in numerical models.

4.3.2 Evaluation of PIV data and comparison to simulated flow velocities

The images obtained from the PIV are evaluated as mentioned in Section 4.2. However, focused on the area of interest in the middle of the microchip, cf. the detail zoomed out in Figure 3, contains regions with significantly different velocities in the channel and neighbouring porous domains. In order to capture the fast moving (free) flow in the channel, every consecutive pair of images is evaluated using the given time delay of 1.4 milliseconds. For evaluating the porous-media flow in the neighbouring porous domains, every tenth image is used with a corresponding time delay of 14 milliseconds. To keep the grid used for the evaluation consistent, the same search area size of 32 px was used for both PIV evaluations. Furthermore, an algorithm is used which averages the velocities in a point-wise manner considering non-consistent zero values. A non-consistent zero value can appear if, for example, no particles are present in a search area window for a given pair of images. In contrast, a consistent zero value would be at locations of the solid inclusion of the porous domain where no particles can physically be present. Given that point-wise averaging algorithm and using thresholds to eliminate outliers and finally superimposing both created velocity fields lead to the contour plot in Figure 16 (right). As a result, it could be shown that the transition region from the faster (free) flow in the channel to the slower (porous-media) flow in the surrounding porous material is in fact occurring within the expected width w_r of roughly half of the unit cell's diagonal, as hypothesised in Section 2.2. Furthermore, the averaged field from the PIV can be compared with the velocity field in Figure 16 (left) obtained from the numerical simulations, which is extracted in the middle of the chip and represents the maximum velocities in the channel. Note that in the three-dimensional simulations, the maximum velocity adjusts in

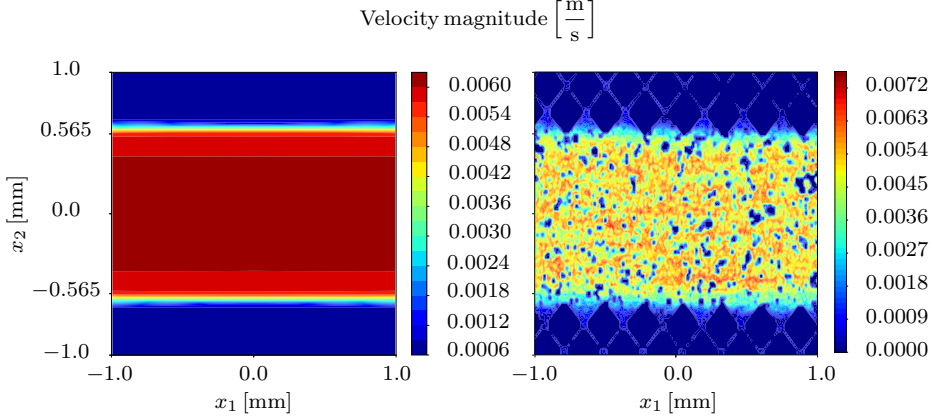


Fig. 16: Comparison of simulated (left) and experimental velocity fields (right)

the middle of the depth of the microchip. Since the velocity field obtained by the PIV measurements is already averaged over the depth (as a consequence of the experimental setup) the simulated velocity needs to be averaged over the depth as well. In the PIV measurements, the no-slip boundary conditions would manifest themselves in an agglomeration of particles on the top and bottom of the PDMS layer which is in reality typically not the case. To adopt this circumstance to the results of the numerical simulations, the influence of the (zero-valued) boundary nodes on the top and bottom walls are neglected accordingly in the averaging process. This leads to the red-coloured simulation curve in Figure 17. To further consider the periodic properties of the studied microfluidic chip, all measured velocities are averaged over the x_1 -direction leading to the blue-coloured experimental curve in Figure 17. In conclusion, it

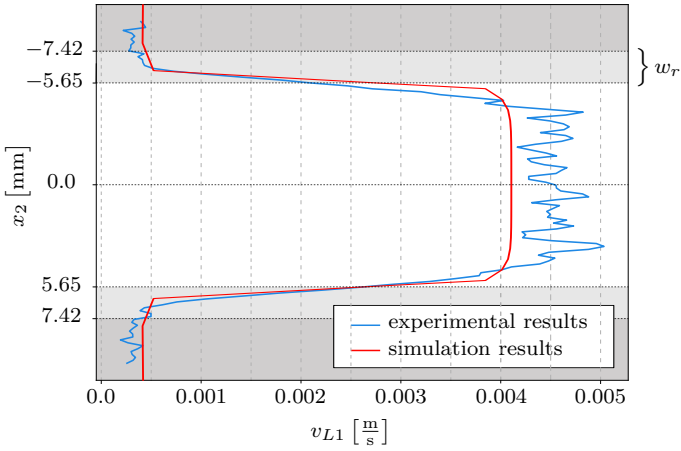


Fig. 17: Velocity profile from averaged velocity field

could be shown that the numerically predicted velocity field is consistent with the experimentally measured velocities. Moreover, with the applied geometrically motivated choice of the length-scale parameter in Section 2.2, the correct slip-length and closely related the correct transition width could be predicted for the given experimental setup.

5 Conclusion

In this work, general theoretical as well as application-oriented aspects are discussed for flow through thin porous materials with an embedded free-flow channel (fracture). In a holistic study of the occurring phenomena, we investigated a combined numerical-experimental approach. For the experimental part of the study, microfluidic chips were used as a suitable choice to study phenomena relevant in sub-surface geo-engineering applications.

At the beginning of this article, the theoretical framework of the biphasic TPM-phase-field model of Ehlers & Luo [13, 14] was introduced with regard to the fluid flow behaviour in a porous material. Therein, we discussed the length-scale parameter ϵ which is responsible for the transition of the phase field. In this regard, we proposed a simple approach to estimate physically meaningful values based on the topological roughness of a material's fracture surface and proposed values for a range of rock materials. The verification of the estimated value was realised by tailored microfluidic experiments, where the experimentally observed transition region is exactly in line with the transition region obtained by the TPM-phase-field simulation. Note that this approach can also be used to determine a meaningful diffuse fracture interface for fracturing processes in single-phasic materials.

In a general study of flow through a thin porous plate containing a free flow channel, we investigated and discussed in analogy to a thin microfluidic sample two different flow scenarios under different boundary conditions and hydraulic conductivities, mimicking sub-surface reservoir conditions. As a highlight arising from the general study, we found that the TPM-phase-field model is capable of capturing even very detailed effects, such as the velocity profile inversion phenomenon. This phenomenon is known from classical channel flow within impermeable walls. With the given model setup, we were able to study the fluid flow in a channel (fracture) with two opposing porous and therefore permeable walls (interfaces) and could show for the first time that this specific effect is increasing for flow into the channel and decreasing for flow out of the channel.

To verify the model assumptions made for the length-scale parameter and to give an example of a real-world application of the TPM phase-field model, we set up microfluidic experiments. As a result of preparatory numerical studies, we could show that the influence of drag or resistance of a channel embedded in a porous domain increases significantly with a decreasing thickness what was interpreted as an effect governed by a reduced distance of the top and bottom walls with a no-slip condition. This emphasises the necessity of

full three-dimensional simulations to accurately capture the nature of physical processes and, furthermore, shows the need for the development of thicker microfluidic devices. For the devices used in this article, we were able to manufacture microfluidic chips with a thickness of roughly $200\text{ }\mu\text{m}$, which is higher as conventional chips. Following that, we discussed the overall experimental setup and evaluation of the pressure and velocity measurements. Therein, the local velocity field for relevant sections of the microfluidic chips were determined using Particle Imaging Velocimetry (PIV).

For model verification, we compared the experimentally obtained data with the numerical results at the example of the microfluidic chip. In this regard, the estimation of the length-scale parameter and the experimentally determined hydraulic conductivities are used as material parameters. In particular, a comparison of discrete inlet pressures and the local velocity field in the middle of the chip showed to be in reasonable agreement. Therefore, the assumptions regarding the length-scale parameter are successfully validated using the velocity field. It was shown, that the diffuse transition width and, closely related, the slip velocities at the porous walls (interfaces) are in good agreement with the experimental results. In conclusion, it has been proven that the TPM-phase-field approach provides an elegant and powerful single-domain approach for the simulation of coupled flow interactions in porous media.

Acknowledgements

Funding: The work is funded by the Deutsche Forschungsgemeinschaft (DFG, German Research Foundation) – SFB 1313 – Project Number 327154368 – Research Projects B02 and Z02 (PML). We would like to thank Michael Neubauer, Stephan Warnat and Andrew Lingley for the fabrication of wafers at the Montana Nanotechnology Facility, an NNCI member supported by NSF Grant ECCS-2025391.

CRediT author statement

Yann Rivas: Conceptualization, Methodology, Software, Formal analysis, Writing - Original Draft, Visualization; **Nikolaos Karadimitriou:** Conceptualization, Methodology, Investigation, Writing - Original Draft; **Holger Steeb:** Conceptualization, Writing - Review & Editing, Supervision, Project administration, Funding acquisition; **Wolfgang Ehlers:** Conceptualization, Methodology, Formal analysis, Writing - Review & Editing, Supervision, Project administration; **Arndt Wagner:** Conceptualization, Methodology, Formal analysis, Writing - Original Draft, Supervision, Project administration, Funding acquisition.

References

1. Adrian, R.J.: Particle-imaging techniques for experimental fluid mechanics. *Annual Review of Fluid Mechanics* **23**, 261–304 (1991). DOI 10.1146/annurev.fl.23.010191.001401
2. Bear, J.: Dynamics of fluids in porous media. American Elsevier, New York (1972)
3. Beavers, G.S., Joseph, D.D.: Boundary conditions at a naturally permeable wall. *Journal of Fluid Mechanics* **30**, 197–207 (1967). DOI 10.1017/S0022112067001375
4. Berre, I., Doster, F., Keilegavlen, E.: Flow in fractured porous media: A review of conceptual models and discretization approaches. *Transport in Porous Media* **130**, 215–236 (2019). DOI 10.1007/s11242-018-1171-6
5. von Böckh, P., Saumweber, C.: Fluidmechanik. Springer (2001)
6. Brinkman, H.C.: A calculation of the viscous force exerted by a flowing fluid on a dense swarm of particles. *Flow, Turbulence and Combustion* **1**, 27–34 (1949). DOI 10.1007/BF02120313
7. Chaaban, M., Heider, Y., Markert, B.: A multiscale LBM–TPM–PFM approach for modeling of multiphase fluid flow in fractured porous media. *International Journal for Numerical and Analytical Methods in Geomechanics* **46**, 2698–2724 (2022). DOI 10.1002/nag.3423
8. Coussy, O.: Poromechanics. John Wiley & Sons (2004)
9. Darcy, H.: Les fontaines publiques de la ville de Dijon: exposition et application des principes à suivre et des formules à employer dans les questions de distribution d'eau, vol. 1. Victor Dalmont (1856)
10. Dastjerdi, S.V., Karadimitriou, N., Hassanzadeh, S.M., Steeb, H.: Experimental evaluation of fluid connectivity in two-phase flow in porous media. *Advances in Water Resources* **172**, 104378 (2023). DOI 10.1016/j.advwatres.2023.104378
11. Ehlers, W.: Foundations of multiphasic and porous materials. In: W. Ehlers, J. Bluhm (eds.) *Porous Media: Theory, Experiments and Numerical Applications*, pp. 3–86. Springer-Verlag, Berlin (2002). DOI 10.1007/978-3-662-04999-0-1
12. Ehlers, W.: Darcy, Forchheimer, Brinkman and Richards: classical hydromechanical equations and their significance in the light of the TPM. *Archive of Applied Mechanics* **22**, 619–639 (2022). DOI 10.1007/s00419-020-01802-3
13. Ehlers, W., Luo, C.: A phase-field approach embedded in the Theory of Porous Media for the description of dynamic hydraulic fracturing. *Computer Methods in Applied Mechanics and Engineering* **315**, 348–368 (2017). DOI 10.1016/j.cma.2016.10.045
14. Ehlers, W., Luo, C.: A phase-field approach embedded in the Theory of Porous Media for the description of dynamic hydraulic fracturing, Part II: The crack-opening indicator. *Computer Methods in Applied Mechanics and Engineering* **341**, 429–442 (2018). DOI 10.1016/j.cma.2018.07.006

15. Ehlers, W., Sonntag, A., Wagner, A.: On hydraulic fracturing in fully and partially saturated brittle porous material. In: F. Aldakheel, B. Hodbivnik, M. Soleimani, H. Wessels, C. Weißenfels, M. Marino (eds.) Current Trends and Open Problems in Computational Mechanics, pp. 111–119. Springer, Cham (2022). DOI 10.1007/978-3-030-87312-7-12
16. Ehlers, W., Wagner, A.: Modelling and simulation methods applied to coupled problems in porous-media mechanics. Archive of Applied Mechanics **89**, 609–628 (2019). DOI 10.1007/s00419-019-01520-5
17. Flekkøy, E., Oxaal, U., Feder, J., Jøssang, T.: Hydrodynamic dispersion at stagnation points: Simulations and experiments. Physical Review E **52**, 4952–4962 (1995). DOI 10.1103/PhysRevE.52.4952
18. Forchheimer, P.: Wasserbewegung durch Boden. Zeitschrift des Vereines Deutscher Ingenieure **45**, 1781–1788 (1901)
19. Fortin, M., Brezzi, F.: Mixed and hybrid finite element methods, vol. 2. Springer-Verlag, New York (1991)
20. Goyeau, B., Lhuillier, D., Gobin, D., Velarde, M.: Momentum transport at a fluid–porous interface. International Journal of Heat and Mass Transfer **46**, 4071–4081 (2003). DOI 10.1016/S0017-9310(03)00241-2
21. Haustein, H.D., Kashi, B.: Distortion of pipe-flow development by boundary layer growth and unconstrained inlet conditions. Physics of Fluids **31**, 063602 (2019). DOI 10.1063/1.5091602
22. Heider, Y., Markert, B.: A phase-field modeling approach of hydraulic fracture in saturated porous media. Mechanics Research Communications **80**, 38–46 (2017). DOI 10.1016/j.mechrescom.2016.07.002
23. Heider, Y., Reiche, S., Siebert, P., Markert, B.: Modeling of hydraulic fracturing using a porous-media phase-field approach with reference to experimental data. Engineering Fracture Mechanics **202**, 116–134 (2018). DOI 10.1016/j.engfracmech.2018.09.010
24. Helmig, R.: Multiphase flow and transport processes in the subsurface: a contribution to the modeling of hydrosystems, vol. 1. Springer Berlin, Heidelberg (1997). DOI 10.1007/978-3-642-60763-9
25. Johnston, I.D., McCluskey, D.K., Tan, C.K., Tracey, M.C.: Mechanical characterization of bulk sylgard 184 for microfluidics and microengineering. Journal of Micromechanics and Microengineering **24**, 035017 (2014). DOI 10.1088/0960-1317/24/3/035017
26. Karadimitriou, N., Joekar-Niasar, V., Hassanzadeh, S., Kleingeld, P., Pyrak-Nolte, L.: A novel deep reactive ion etched (DRIE) glass micro-model for two-phase flow experiments. Lab on a Chip **12**, 3413–3418 (2012). DOI 10.1039/C2LC40530J
27. Karadimitriou, N., Musterd, M., Kleingeld, P., Kreutzer, M., Hassanzadeh, S., Joekar-Niasar, V.: On the fabrication of PDMS micromodels by rapid prototyping, and their use in two-phase flow studies. Water Resources Research **49**, 2056–2067 (2013). DOI 10.1002/wrcr.20196
28. Krach, D., Ruf, M., Steeb, H.: POREMAPS: A finite difference based Porous Media Anisotropic Permeability Solver for Stokes flow (2024). URL <https://arxiv.org/abs/2407.19868>

-
29. Krach, D., Weinhardt, F., Wang, M., Schneider, M., Class, H., Steeb, H.: A novel geometry-informed drag term formulation for pseudo-3D Stokes simulations with varying apertures. *Advances in Water Resources* **195**, 104860 (2025). DOI 10.1016/j.advwatres.2024.104860
30. Kuhn, C., Müller, R.: A continuum phase field model for fracture. *Engineering Fracture Mechanics* **77**, 3625–3634 (2010). DOI 10.1016/j.engfracmech.2010.08.009
31. Lobo, O.J., Chatterjee, D.: Effect of aspect ratio on entrance length in rectangular minichannels with plenum. *Physics of Fluids* **34**, 112009 (2022). DOI 10.1063/5.0119897
32. Miehe, C., Hofacker, M., Welschinger, F.: A phase field model for rate-independent crack propagation: Robust algorithmic implementation based on operator splits. *Computer Methods in Applied Mechanics and Engineering* **199**, 2765–2778 (2010). DOI 10.1016/j.cma.2010.04.011
33. Miehe, C., Welschinger, F., Hofacker, M.: Thermodynamically consistent phase-field models of fracture: Variational principles and multi-field FE implementations. *International Journal for Numerical Methods in Engineering* **83**, 1273–1311 (2010). DOI 10.1002/nme.2861
34. Mlynarczuk, M.: Description and classification of rock surfaces by means of laser profilometry and mathematical morphology. *International Journal of Rock Mechanics and Mining Sciences* **47**, 138–149 (2010). DOI 10.1016/j.ijrmms.2009.09.004
35. Reci, A., Sederman, A., Gladden, L.: Experimental evidence of velocity profile inversion in developing laminar flow using magnetic resonance velocimetry. *Journal of Fluid Mechanics* **851**, 545–557 (2018). DOI 10.1017/jfm.2018.512
36. Rybak, I., Schwarzmeier, C., Eggenweiler, E., Rüde, U.: Validation and calibration of coupled porous-medium and free-flow problems using pore-scale resolved models. *Computational Geosciences* **25**, 621–635 (2021). DOI 10.1007/s10596-020-09994-x
37. Saffman, P.G.: On the boundary condition at the surface of a porous medium. *Studies in Applied Mathematics* **50**, 93–101 (1971). DOI 10.1002/sapm197150293
38. Sigloch, H.: *Technische Fluidmechanik*, vol. 1. Springer (1991)
39. Silva, R.A., de Lemos, M.J.: Numerical analysis of the stress jump interface condition for laminar flow over a porous layer. *Numerical Heat Transfer: Part A: Applications* **43**, 603–617 (2003). DOI 10.1080/10407780307351
40. Silva, R.A., de Lemos, M.J.: Turbulent flow in a channel occupied by a porous layer considering the stress jump at the interface. *International Journal of Heat and Mass Transfer* **46**, 5113–5121 (2003). DOI 10.1016/S0017-9310(03)00368-5
41. Sonntag, A., Wagner, A., Ehlers, W.: Dynamic hydraulic fracturing in partially saturated porous media. *Computer Methods in Applied Mechanics and Engineering* **414**, 116121 (2023). DOI 10.1016/j.cma.2023.116121
42. Strohbeck, P., Eggenweiler, E., Rybak, I.: A modification of the beavers–joseph condition for arbitrary flows to the fluid–porous interface. *Trans-*

- port in Porous Media **147**, 605–628 (2023). DOI 10.1007/s11242-023-01919-3
43. Terzis, A., Zarikos, I., Weishaupt, K., Yang, G., Chu, X., Helmig, R., Weigand, B.: Microscopic velocity field measurements inside a regular porous medium adjacent to a low reynolds number channel flow. *Physics of Fluids* **31**, 042001 (2019). DOI 10.1063/1.5092169
44. Valdés-Parada, F.J., Goyeau, B., Ochoa-Tapia, J.A.: Diffusive mass transfer between a microporous medium and an homogeneous fluid: Jump boundary conditions. *Chemical Engineering Science* **61**, 1692–1704 (2006). DOI 10.1016/j.ces.2005.10.005
45. Wagner, A., Eggenweiler, E., Weinhardt, F., Trivedi, Z., Krach, D., Lohrmann, C., Jain, K., Karadimitriou, N., Bringedal, C., Voland, P., Holm, C., Class, H., Steeb, H., Rybak, I.: Permeability estimation of regular porous structures: A benchmark for comparison of methods. *Transport in Porous Media* **138**, 1–23 (2021). DOI 10.1007/s11242-021-01586-2
46. Wagner, A., Sonntag, A., Reuschen, S., Nowak, W., Ehlers, W.: Hydraulically induced fracturing in heterogeneous porous media using a TPM-phase-field model and geostatistics. *Proceedings in Applied Mathematics and Mechanics* **23**, e202200118 (2023). DOI <https://doi.org/10.1002/pamm.202200118>
47. Wang, J., Sonntag, A., Lee, D., Xotta, G., Salomoni, V.A., Steeb, H., Wagner, A., Ehlers, W.: Modelling and simulation of natural hydraulic fracturing applied to experiments on natural sandstone cores. *Acta Geotechnica* **19**, 7709–7725 (2024). DOI 10.1007/s11440-024-02351-7
48. Weishaupt, K., Terzis, A., Zarikos, I., Yang, G., Flemisch, B., de Winter, D., Helmig, R.: A hybrid-dimensional coupled pore-network/free-flow model including pore-scale slip and its application to a micromodel experiment. *Transport in Porous Media* **135**, 243–270 (2020). DOI 10.1007/s11242-020-01477-y
49. Xia, Y., Whitesides, G.M.: Soft Lithography. *Annual Review of Materials Science* **28**, 153–184 (1998). DOI 10.1146/annurev.matsci.28.1.153